Journal of Power Sources 245 (2014) 331–336

Contents lists available at SciVerse ScienceDirect

Journal of Power Sources

journal homepage: www.elsevier.com/locate/jpowsour

Short communication

The influence of temperature on a nutty-cake structural material: $LiMn_{1-x}Fe_xPO_4$ composite with $LiFePO_4$ core and carbon outer layer for lithium-ion battery

Zhen-Qing Huo, Yu-Ting Cui, Dan Wang, Yue Dong, Li Chen*

Department of Chemistry, Tianjin University, Tianjin 300072, People's Republic of China

HIGHLIGHTS

- A nutty-cake structural C–$LiMn_{1-x}Fe_xPO_4$–$LiFePO_4$ cathode material is synthesized.
- The calcination temperature has obvious influence on the crystal structure.
- Fe^{2+} diffused from the $LiFePO_4$ core to the outer $LiMnPO_4$ layer during calcination.

ARTICLE INFO

Article history:
Received 28 March 2013
Received in revised form
26 June 2013
Accepted 26 June 2013
Available online 4 July 2013

Keywords:
Cathode material
Ion diffusion
Nutty-cake structure
Lithium-ion batteries

ABSTRACT

The extremely low electronic conductivity, slow ion diffusion kinetics, and the Jahn–Teller effect of $LiMnPO_4$ limit its electrochemical performance. In this work, a nutty-cake structural C–$LiMn_{1-x}Fe_xPO_4$–$LiFePO_4$ cathode material is synthesized by hydrothermal method and further calcined at different temperatures. The influence of calcination temperature on the electrochemical behavior is investigated by X-ray diffractometer, scanning electron microscope, field-emission high-resolution transmission electron microscope, energy-dispersive X-ray spectroscopy, electrochemical impedance spectroscopy and charge–discharge tests. And the performance of C–$LiMn_{1-x}Fe_xPO_4$–$LiFePO_4$ materials has a relationship with its crystal structure. The well-crystallized Sample-600 calcined at 600 °C shows the smallest charge transfer resistance, the largest lithium ion diffusion coefficient (D_{Li}) and the best cycling stability. The discharge capacity of Sample-600 holds around 112 mAh g^{-1} after the 3rd cycle at 0.1 C rate. The performances improvement of C–$LiMn_{1-x}Fe_xPO_4$–$LiFePO_4$ material can be mainly attributed to the iron diffusion from the $LiFePO_4$ core to the outer $LiMnPO_4$ layer under appropriate calcination temperature.

1. Introduction

Olivine framed lithium metal phosphates [$LiMPO_4$ (M = Fe, Mn, Ni, and Co)] have recently attracted much attention as a potential cathode material for Li-ion battery due to their high safety, environment friendly nature, low cost, high thermal stability and high theoretical capacity (170 mAh g^{-1}) [1–5]. In the olivine family, $LiMnPO_4$ is another promising cathode material beside $LiFePO_4$, which can give a higher voltage of 4.2 V ($LiFePO_4$: 3.5 V) *vs.* Li/Li^+ and a higher theoretical energy density 684 Wh kg^{-1} ($LiFePO_4$: 578 Wh kg^{-1}) [1], but the electronic conductivity of $LiMnPO_4$ ($<10^{-10}$ S cm^{-1}) is much lower than that of $LiFePO_4$ (1.8×10^{-9} S cm^{-1}) [6,7]. The intrinsically low ionic and electronic conductivity of $LiMnPO_4$ has limited its practical application in high power batteries, and the Jahn–Teller distortion associated with Mn^{3+} also hinders the real application of $LiMnPO_4$. During cycling, the shrinkage of $LiMnPO_4$ is about 8.9%, but only 6.8% for $LiFePO_4$ [8].

The effective methods to improve the electrochemical performance of $LiMnPO_4$ include Mn-site doping [9–11], particle size minimization [12–14] and carbon coating [15,16]. Appropriate substitution iron for Mn is beneficial to produce small volume change of $LiMnPO_4$ during lithium extraction/insertion [8]. Further coating an electronically conducting phase is helpful to improve the poor electronic conductivity of $LiMnPO_4$. The $LiMnPO_4$ particles coating with $LiFePO_4$ and C has been reported by K. Zaghib et al. [17]. The carbon-coated $LiFePO_4$–$LiMnPO_4$ composite shows better electrochemical properties than the carbon-coated $LiMn_{2/3}Fe_{1/3}PO_4$ with the same composition. It is well known that the electronic conductivity and ionic conductivity of $LiMnPO_4$ is much lower than

* Corresponding author. Tel.: +86 22 27892379; fax: +86 22 27403475.
E-mail address: chenli_su@eyou.com (L. Chen).

0378-7753/$ – see front matter © 2013 Elsevier B.V. All rights reserved.
http://dx.doi.org/10.1016/j.jpowsour.2013.06.148

that of $LiFePO_4$ [6,7]. The outward diffusion of Li^+ from the center of $LiMnPO_4$ particles should be more difficult, thus the electrochemical properties of internal $LiMnPO_4$ are severely hindered. At the same time, the dissolution of Fe^{2+} from $LiFePO_4$ is almost inevitable [18] which would lead to internal short circuit and low open circuit voltage of the battery. To solve those problems, a $Li(Mn,Fe)PO_4$ composite with $LiFePO_4$ core and a carbon outer layer is prepared to study its electrochemical properties in the present work.

2. Experimental details

2.1. Preparation of $LiFePO_4$

$LiFePO_4$ was synthesized by a hydrothermal route from starting materials $FeSO_4 \cdot 7H_2O$, H_3PO_4, and $LiOH \cdot H_2O$ in a molar ratio of 1:1:3. A 0.35 mol L^{-1} H_3PO_4 aqueous solution and a 0.35 mol L^{-1} $FeSO_4$ aqueous solution were mixed with vigorous agitation firstly, then a 1.05 mol L^{-1} LiOH solution was added drop-wise to the above solution. After stirring for 5 min under Ar atmosphere, the suspension was transferred into a hydrothermal autoclave reactor, heated at 220 °C for 7 h. After naturally cooling to room temperature, the $LiFePO_4$ powder was filtered, washed with water and ethanol for several times, and then dried at 80 °C in vacuum.

2.2. Coating with $LiMnPO_4$

Firstly, a 0.35 mol L^{-1} H_3PO_4 aqueous solution was mixed with a 0.35 mol L^{-1} $MnSO_4$ aqueous solution with vigorous agitation, then a 1.05 mol L^{-1} LiOH solution was added drop-wise into the above solution to obtain the precursor solution with a Li:Mn:P molar ratio of 3:1:1. Then $LiFePO_4$ prepared in step 2.1 and the precursor solution were mixed with a Mn:Fe molar ratio of 4:1 and added into a PTFE vessel again, and the subsequent process was the same as that described in step 2.1.

2.3. Carbon-coating

The composite obtained at the end of step 2.2 was mixed with a sucrose solution, and the weight ratio of composite/sucrose was 10:1. The mixture $LiMnPO_4$–$LiFePO_4$ was dried at 60 °C under vacuum firstly, then the mixture was heated at 300 °C for 1 h to carbonize the sucrose, and calcined at 550 °C, 600 °C and 650 °C for 3 h respectively under Ar gas flow to form C–$LiMn_{1-x}Fe_xPO_4$–$LiFePO_4$ composite named as Sample-550, Sample-600, Sample-650 respectively.

2.4. Apparatus

Thermo-gravimetric and differential scanning calorimetry (TG–DSC) analyses were used to understand the phase transformation of synthesized composite powder using a simultaneous thermal analyzer (STA 409 PC/PG, NETZSCH). The powder was heated from room temperature to 900 °C under N_2 atmosphere at a heating rate of 10 °C min^{-1}. X-ray diffraction analysis was carried out using a X-ray diffractometer (XRD, D/max 2500 V/PC, Rigaku, 40 KV, 150 mA) using Cu Kα radiation and a graphite monochromator. The samples were scanned over the 10–90° (2θ) range at a scan speed of 2°min^{-1} (step size 0.02°, step time 0.6 s). Morphology and external components of the samples were investigated using a scanning electron microscope (SEM, XL30, Philips) with an energy-dispersive X-ray spectroscopy (EDX). The interior structure of the samples was observed by a field-emission high-resolution transmission electron microscope (HRTEM, JEM-2100F, JEOL) with an energy-dispersive X-ray spectroscopy (EDX). Electrochemical impedance spectroscopy (EIS, Zennium, Zhaner Elektrik) was carried out in a frequency range from 0.1 Hz to 100 kHz with an AC signal of 5 mV.

The cathode was prepared by coating a viscous slurry with 80% C–$LiMn_{1-x}Fe_xPO_4$–$LiFePO_4$ composite, 10% conductive carbon black (Super P), and 10% polyvinylidene fluoride (PVDF) binder onto Al foils. The cathode was dried at 120 °C for 12 h to gain a coating layer with 150 μm. A mixture of ethylene carbonate (EC) and dimethyl carbonate (DEC) (volume ratio = 1:1) containing 1 M $LiPF_6$ was used as the electrolyte. All cells were assembled in an argon-filled glove box. The electrochemical properties of the cathodes were measured by a battery testing system (CT2001A, LAND) at a current density of 0.1 C rate (1 C = 170 mA g^{-1}) between 2.5 and 4.5 V *vs.* Li/Li^+ at room temperature.

3. Results and discussion

TG/DSC curves could help confirm the annealing program of precursor mixtures. Fig. 1 shows the TG/DSC curves of precursor mixtures. The TG curve exhibits a single weight loss stage about 5.58 wt. % between 180 °C and 300 °C, and there is no significant weight loss after 300 °C. The percent weight loss is mainly ascribed to the dehydration of sucrose [19,20], which is in accordance with the theoretical value (5.26 wt.%). However, a sharp endothermic DSC peak is observed at around 600 °C, which indicates that a solid solution $LiMn_{1-x}Fe_xPO_4$ *via* crystalline substitution is formed in this range. The supposition is proved further by the following detection technology.

Fig. 2(a) shows XRD pattern of $LiFePO_4$ synthesized in step 2.1. The diffraction peaks confirm the formation of the pure and well-crystallized $LiFePO_4$ with an orthorhombic olivine structure, and the pattern matches well with the standard $LiFePO_4$ (PDF#40-1499). Fig. 2(b) shows the XRD patterns and the inset shows the local enlarged XRD patterns between $2\theta = 50°$–$55°$. The JCPDS card data of $Li(Mn,Fe)PO_4$ (PDF#13-0336) and $LiMnPO_4$ (PDF#33-0804) are also shown in Fig. 2(b). All three samples are ordered olivine compounds with an orthorhombic structure (space group Pnma) and which is similar to that of $LiMnPO_4$, and $Li(Mn,Fe)PO_4$. Because the lattice parameters of $LiFePO_4$ and $LiMnPO_4$ are close, the XRD patterns show delicate difference only at high angle [17].

The inset shows the peaks shift slightly to higher angles with increasing calcination temperature. A small peak splitting is also observed around 52° only at 550 °C which disappears at temperatures higher than 600 °C. The crystal structure determined from XRD patterns by means of FOM value suggests that the samples at

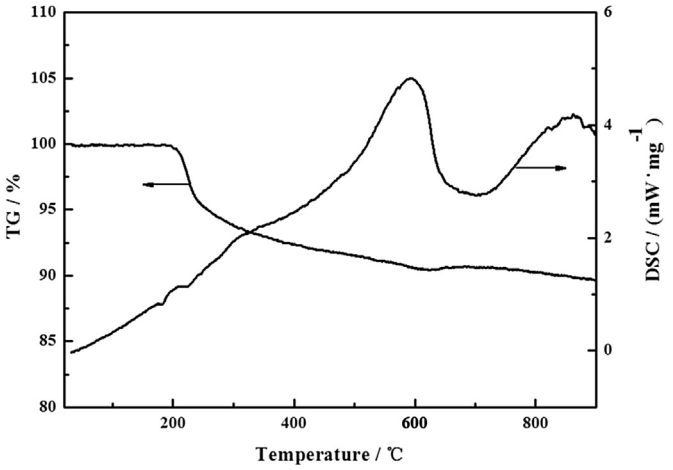

Fig. 1. TG/DSC curves of precursor mixtures.

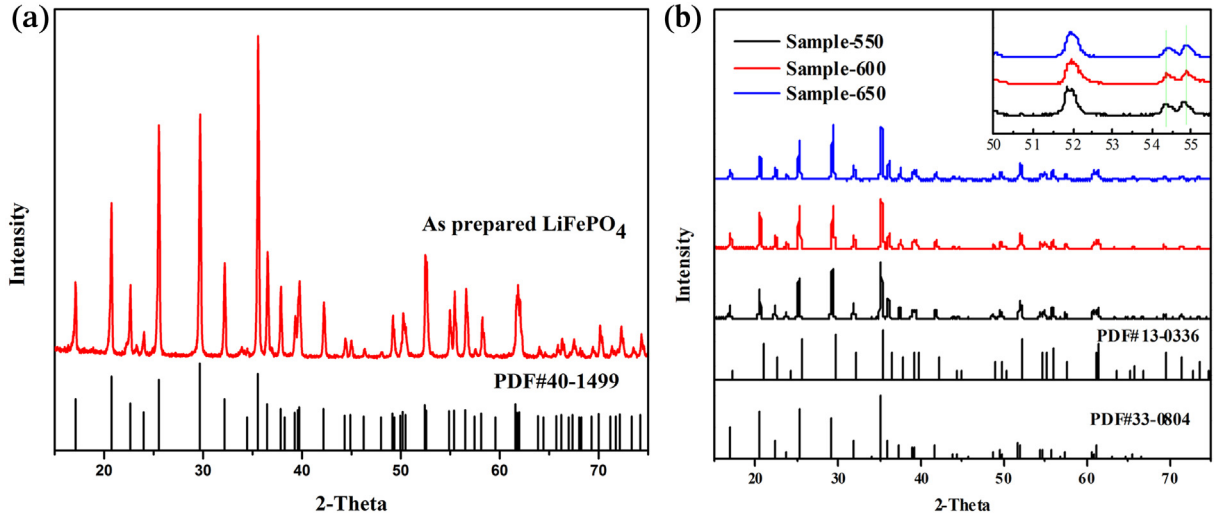

Fig. 2. XRD patterns of (a) synthesized $LiFePO_4$ and (b) Sample-550, Sample-600 and Sample-650, (inset: Partially enlarged XRD patterns of samples).

Table 1
Refined cell parameters for the samples.

Sample	*a* (Å)	*b* (Å)	*c* (Å)	Volume (Å)
Sample-550	6.09216	10.44277	4.74087	301.61
Sample-600	6.08649	10.43461	4.7396	301.01
Sample-650	6.07924	10.42193	4.7379	299.79

600 °C and 650 °C can be well indexed with single-phase orthorhombic Pmnb similar to $Li(Mn,Fe)PO_4$ (PDF#13-0336), but the sample at 550 °C had to be indexed with $LiMnPO_4$ (PDF#33-0804). From this, we could assume that the $LiFePO_4$ core and the $LiMnPO_4$ out layer could form a solid solution of $LiMn_{1-x}Fe_xPO_4$ when the temperature is higher than 600 °C, but the melt migration is incomplete when the partial melting happens at 550 °C. At the same time, little $LiFePO_4$ grains in the carbon-coated $LiMn_{1-x}Fe_xPO_4$–$LiFePO_4$ composite have less influence on the XRD patterns of $LiMnPO_4$. The absence of carbon peak in the patterns indicates that not only the lower carbon content but also the low crystallinity of carbon pyrolyzed from sucrose [9].

Table 1 shows the lattice constants of samples. The lattice constants *a*, *b*, *c* and the volume all decrease with the increase of calcination temperature. The lattice change can be ascribed to the substitution of larger Mn^{2+} (0.67 Å) by smaller Fe^{2+} (0.61 Å) [21].

Fig. 3 shows the SEM images and EDX spectra of samples. The SEM images of Sample-550 and Sample-600 in Fig. 3(a) and (b) exhibits loose particles with a relatively uniform size distribution, but Sample-650 in Fig. 3(d) forms large particles which are mostly caused by the higher calcination temperature. It is well known that the loose microstructure can facilitate better penetration of electrolyte into the material and further improve ion diffusion inside

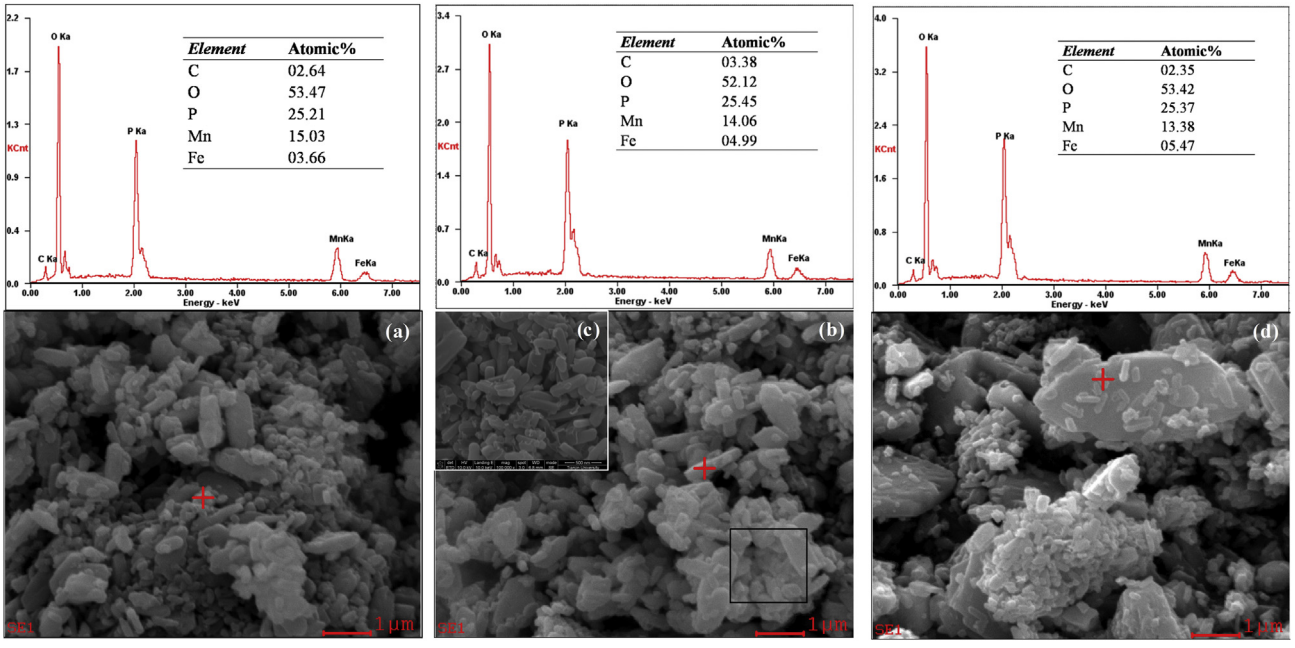

Fig. 3. EDX spectrum and SEM image of the C–$LiMn_{1-x}Fe_xPO_4$–$LiFePO_4$ composite (a) Sample-550 (b), Sample-600, (c) enlarged view of (b), (d) Sample-650.

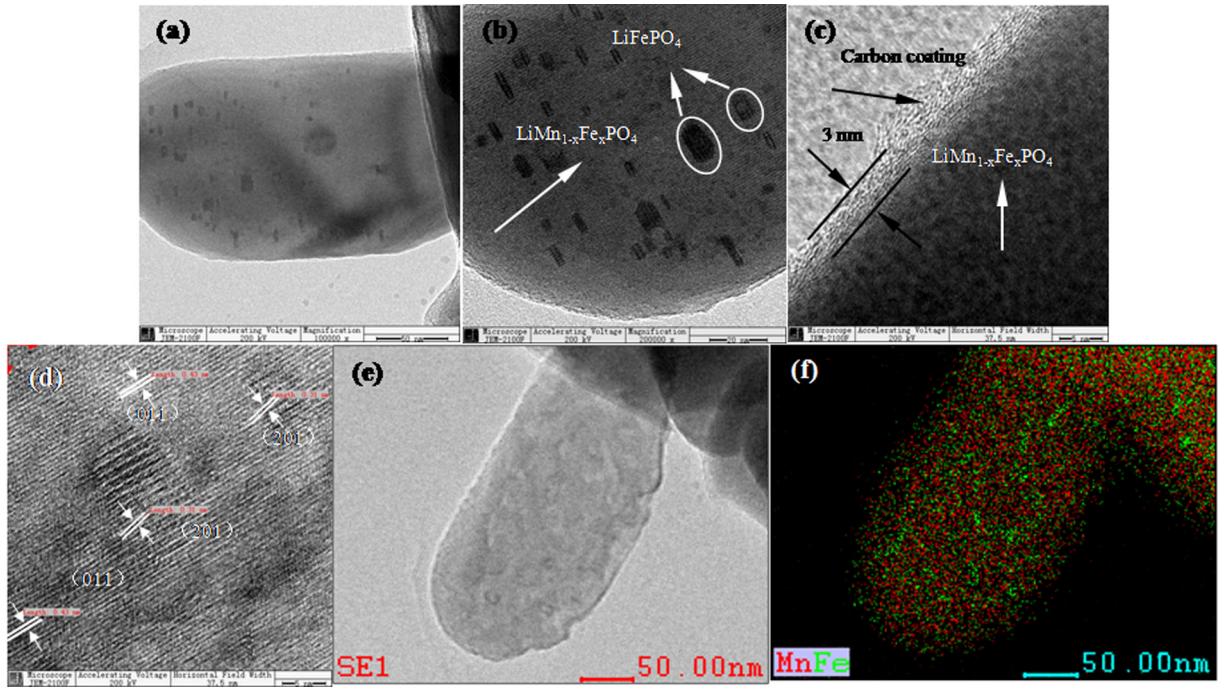

Fig. 4. HRTEM images (a), (b), (c), (d) and EDX map (f) of (e) for Sample-600.

the material. The enlarged view of Sample-600 in Fig. 3(c) apparently exhibits rod-like particles. The powder particle size and the Fe/Mn ratio on the surface of particles both increase with increasing temperature, from which we could infer that Fe^{2+} in the $LiFePO_4$ core tends to diffuse into the outer $LiMnPO_4$ layer in the calcining process. The EDX conclusions are in good accordance with our previous XRD results.

TEM images and EDX map in Fig. 4 can be used to further investigate the microstructure and carbon coating of C–$LiMn_{1-x}Fe_xPO_4$–$LiFePO_4$ samples. The enlarged images (b) of Fig. 4(a) shows that a number of small $LiFePO_4$ particles uniformly embed into $LiMn_{1-x}Fe_xPO_4$ to form a nutty-cake structure [22] material, in which the size of $LiFePO_4$ core (about 15 nm) is less than the size of the intermediate products (about 50 nm, calculated by the Scherrer formula) prepared *via* hydrothermal method in step 2.1. It is overly optimistic to assume that the diffusion of Fe^{2+} into the outer $LiMnPO_4$ layer in the calcining process leads to the formation of $LiMn_{1-x}Fe_xPO_4$ solid solution. A uniform carbon coating with a thickness of about 3 nm on the outside of $LiMn_{1-x}Fe_xPO_4$ in Fig. 4(c) is also observed. Fig. 4(d) is the further enlarged view of Fig. 4(b), which shows clear lattice fringes images of $LiFePO_4$ and $LiMn_{1-x}Fe_xPO_4$. The lattice fringe with a width of 0.31 nm corresponds to the (201) plane of $LiFePO_4$ [23], and that of 0.43 nm corresponds to the (011) plane of $LiMn_{1-x}Fe_xPO_4$ [8]. The difference in lattice spacings indicates that the particle includes a $LiFePO_4$ core and $LiMn_{1-x}Fe_xPO_4$ out layer. The EDX map (f) of (e) verifies that smaller $LiFePO_4$ particles uniformly embed into $LiMn_{1-x}Fe_xPO_4$ at a nanostructural scale.

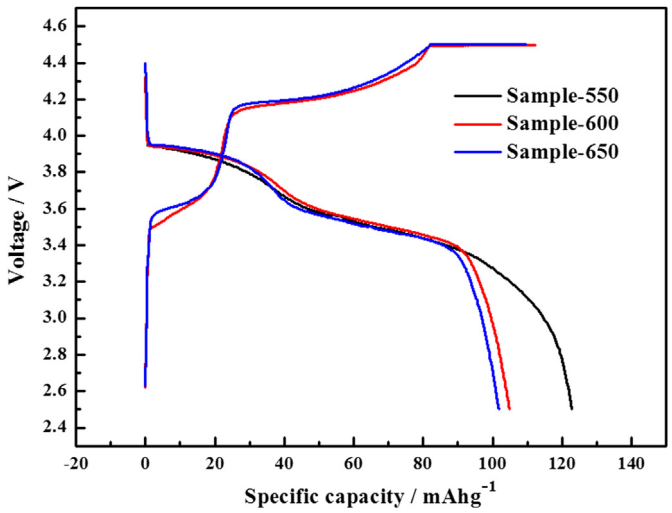

Fig. 5. Charge/discharge curves of 1st cycle at 0.1 C rate for Sample-550, Sample-600 and Sample-650.

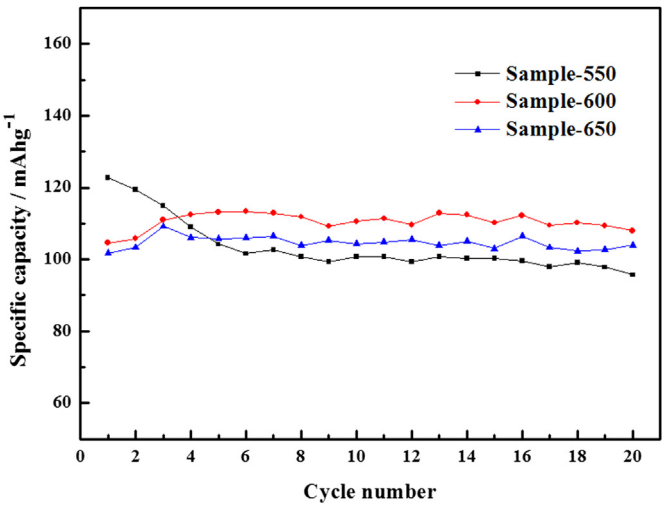

Fig. 6. Discharge specific capacities at 0.1 C rate for Sample-550, Sample-600 and Sample-650.

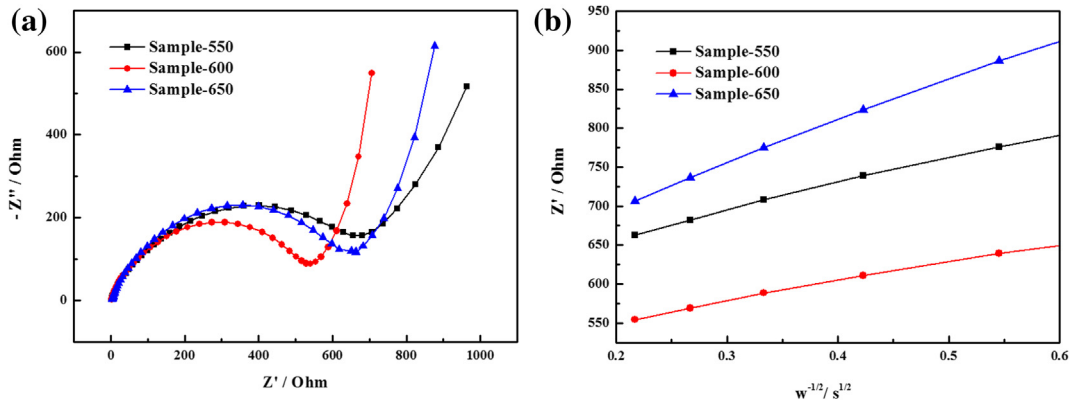

Fig. 7. (a) AC impedance spectra of samples, and (b) the relationship between Z′ and $\omega^{-1/2}$ in low frequency region.

Fig. 5 presents the charge/discharge curves of 1st cycle at 0.1 C rate for samples. The cells are charged to 4.5 V under a CC–CV protocol at 0.1 C rate firstly, held at 4.5 V until the current decreased to 0.01 C, then discharged to 2.5 V at 0.1 C rate. All samples exhibit two charge/discharge plateaus around 4.0 V and 3.5 V *vs.* Li/Li^+ corresponding to the redox couples Mn^{2+}/Mn^{3+} and Fe^{2+}/Fe^{3+} [24] respectively. With the increase of calcination temperature, the charge voltage plateaus corresponding to Mn^{2+}/Mn^{3+} become shorter, but the charge voltage plateaus corresponding to Fe^{2+}/Fe^{3+} becomes longer. There is almost no obvious charge voltage plateau corresponding to Fe^{2+}/Fe^{3+} in Sample-550. The differences in charge voltage plateau are related to the change of crystal structure of samples. All the diffraction peaks of Sample-550 could be clearly indexed as olivine-type $LiMnPO_4$, while all the diffraction peaks of Sample-600 and Sample-650 are clearly indexed as $Li(Mn,Fe)PO_4$. The discharge specific capacity is 122.8 mAh g^{-1} for Sample-550, 104.6 mAh g^{-1} for Sample-600 and 101.8 mAh g^{-1} for Sample-650. The discharge specific capacities for samples decrease obviously with increasing temperature, which is related to the particle agglomeration at higher temperature. Carbon coating has less influence on the performance of composite [25].

Fig. 6 shows the discharge specific capacities at 0.1 C rate. The capacity difference reveals that the diversity of crystal structure originating from calcination temperature has obvious influence on sample's performance. Although Sample-550 shows the highest initial discharge capacity of 122.8 mAh g^{-1}, it falls rapidly to 105 mAh g^{-1} after the 6th cycle. We conclude that the initial capacity fade of Sample-550 is due to the Jahn–Teller distortion [26,27] which could induce volume and cell distortion. As a result, the rapid mechanical degradation of the electrode directly leads to the rapid capacity fade during the charge/discharge process. As for Sample-600 and Sample-650, the discharge capacity of 1st cycle is lower, but the capacities become higher after the 2nd cycle, and the discharge capacity of Sample-600 tends to hold around 112 mAh g^{-1} after the 3rd cycle, which is higher than the previously reported value (about 108 mAh g^{-1} for C–$LiFePO_4$–$LiMnPO_4$ and 54.5 mAh g^{-1} for $LiMn_{2/3}Fe_{1/3}PO_4$/C at 0.1 C rate) by K. Zaghib et al. [17]. We assume that the better discharge capacity of Sample-600 is mainly attributed to the improved ionic and electronic conductivity of the synthesized composite $LiMn_{1-x}Fe_xPO_4$.

AC impedance spectra are measured to further verify the influence of calcination temperature on samples. The spectra of samples in Fig. 7(a) all have similar profiles which are composed of a semicircle in the high-to-medium frequency region and an inclined line in the low frequency region. The semicircle is approximately related to the charge transfer process, and the inclined line is associated with the Li^+ diffusion. Lithium ion diffusion coefficient (D_{Li}) can be roughly calculated from the following Equation (1) [9,28,29]:

$$D = \frac{R^2T^2}{2A^2n^4F^4C^2\sigma^2} \tag{1}$$

where R is the gas constant, T the absolute temperature, A the surface area of the electrode, n the number of electrons per molecule during oxidization, F the Faraday's constant and C the molar concentration of Li^+, σ the Warburg factor which can be obtained by Equation (2):

$$Z' = R_e + R_{ct} + \sigma\omega^{-1/2} \tag{2}$$

Where R_e is the resistance of electrolyte, R_{ct} is the charge transfer resistance and ω is the angular frequency. Both R_e and R_{ct} are independent of frequency. ω obtained from the plot slope of Z' *vs.* $\omega^{-1/2}$ as shown in Fig. 7 (b). Clearly, Sample-600 with the smallest semicircle gives the smallest charge transfer resistance. When the Li^+ concentration adopts 2.67×10^{-3} mol cm^{-3} in the study, the D_{Li} at 550 °C, 600 °C and 650 °C is 2.77×10^{-14} cm^2 s^{-1}, 5.15×10^{-14} cm^2 s^{-1} and 1.06×10^{-14} cm^2 s^{-1}, respectively, which are higher than the value of 1.69×10^{-15} cm^2 s^{-1} for pure $LiMnPO_4$ [9]. The largest D_{Li} value of Sample-600 indicates that the fastest lithium diffusion rate can be obtained at 600 °C in the C–$LiMn_{1-x}Fe_xPO_4$–$LiFePO_4$ composite. The result further confirms that the calcination temperature has obvious influence on electrochemical behavior.

The importance of Fe/Mn ratio to the $LiFe_{1-x}Mn_xPO_4$ samples' properties has also been reported elsewhere [8]. More efforts should be focused on the optimization of Fe/Mn ratio to improve the property of C–$LiMn_{1-x}Fe_xPO_4$–$LiFePO_4$ further in the future.

4. Conclusion

In this work, we have presented a nutty-cake structural C–$LiMn_{1-x}Fe_xPO_4$–$LiFePO_4$ cathode material with an orthorhombic structure of $Li(Mn,Fe)PO_4$. The calcination temperature has obvious influence on the crystal structure of $LiMnPO_4$–$LiFePO_4$. The well-crystallized Sample-600 with the smallest charge transfer resistance and the largest lithium ion diffusion coefficient (D_{Li}) shows the best cycling stability, which holds a stable discharge capacity around 112 mAh g^{-1} after the 3rd cycle at 0.1 C rate. The performances improvement of C–$LiMn_{1-x}Fe_xPO_4$–$LiFePO_4$ material can be mainly attributed to the iron diffusion from the $LiFePO_4$ core to the outer $LiMnPO_4$ layer under appropriate calcination temperature.

Acknowledgments

The authors acknowledge the support of Tianjin B&M Science and Technology Joint-Stock Co., Ltd.

References

[1] A.K. Padhi, K.S. Nanjundaswamy, J.B. Goodenough, J. Electrochem. Soc. 144 (1997) 1188–1194.
[2] G. Li, H. Azuma, M. Tohda, Electrochem. Solid-State Lett. 5 (2002) A135–A137.
[3] M.S. Islam, D.J. Driscoll, C.A.J. Fisher, P.R. Slater, Chem. Mater. 17 (2005) 5085–5092.
[4] B. Kang, G. Ceder, Nature 458 (2009) 190–193.
[5] J. Wolfenstine, J. Allen, J. Power Sources 136 (2004) 150–153.
[6] M. Yonemura, A. Yamada, Y. Takei, N. Sonoyama, R. Kanno, J. Electrochem. Soc. 151 (2004) A1352–A1356.
[7] C. Delacourt, L. Laffont, R. Bouchet, C. Wurm, J.-B. Leriche, M. Morcrette, J.-M. Tarascon, C. Masquelier, J. Electrochem. Soc. 152 (2005) A913–A921.
[8] L. Chen, Y. Yuan, X. Feng, M. Li, J. Power Sources 214 (2012) 344–350.
[9] H. Fang, H. Yi, C. Hu, B. Yang, Y. Yao, W. Ma, Y. Dai, Electrochim. Acta 71 (2012) 266–269.
[10] Z. Wang, L. Yuan, W. Zhang, Y. Huang, J. Alloys Compd. 532 (2012) 25–30.
[11] Z. Yang, G. Cao, J. Xie, X. Zhao, J. Solid State Electrochem. 16 (2012) 1271–1277.
[12] M. Pivko, M. Bele, E. Tchernychova, N.Z. Logar, R. Dominko, M. Gaberscek, Chem. Mater. 24 (2012) 1041–1047.
[13] N.H. Kwon, K.M. Fromm, Electrochim. Acta 69 (2012) 38–44.
[14] F. Wang, J. Yang, P. Gao, Y. NuLi, J. Wang, J. Power Sources 196 (2011) 10258–10262.
[15] S. Moon, P. Muralidharan, D.K. Kim, Ceram. Int. 38 (2012) S471–S475.
[16] P.R. Kumar, M. Venkateswarlu, M. Misra, A.K. Mohanty, N. Satyanarayana, J. Electrochem. Soc. 158 (2011) A227–A230.
[17] K. Zaghib, M. Trudeau, A. Guerfi, J. Trottier, A. Mauger, R. Veillette, C.M. Julien, J. Power Sources 204 (2012) 177–181.
[18] K. Amine, J. Liu, I. Belharouak, Electrochem. Commun. 7 (2005) 669–673.
[19] G.N. Richards, F. Shafizadeh, Aust. J. Chem. 31 (1978) 1825–1832.
[20] E.-H.M. Diefallah, Thermochim. Acta 202 (1992) 1–16.
[21] J.Z. Zou, Q.G. Fu, X.R. Zeng, F. Deng, Y. Yan, Key Eng. Mater. 519 (2012) 124–127.
[22] L.W. Su, Y. Jing, Z. Zhou, Nanoscale 3 (2011) 3967–3983.
[23] S. Lim, C.S. Yoon, J. Cho, Chem. Mater. 20 (2008) 4560–4564.
[24] K.W. Nam, X.J. Wang, W.-S. Yoon, H. Li, X. Huang, O. Haas, J. Bai, X.Q. Yang, Electrochem. Commun. 11 (2009) 913–916.
[25] S.K. Martha, J. Grinblat, O. Haik, E. Zinigrad, T. Drezen, J.H. Miners, I. Exnar, A. Kay, B. Markovsky, D. Aurbach, Angew. Chem. Int. Ed. 48 (2009) 8559–8563.
[26] A. Yamada, S.C. Chung, K. Hinokuma, J. Electrochem. Soc. 148 (2001) A224–A229.
[27] Z.X. Nie, C.Y. Ouyang, J.Z. Chen, Z.Y. Zhong, Y.L. Du, S.Q. Shi, M.S. Lei, Solid State Commun. 150 (2010) 40–44.
[28] H. Liu, C. Li, H.P. Zhang, L.J. Fu, Y.P. Wu, H.Q. Wu, J. Power Sources 159 (2006) 717–720.
[29] Y. Cui, X. Zhao, R. Guo, Electrochim. Acta 55 (2010) 922–926.